Multi-Objective Hypersonic Entry Aeroshell Shape Optimization

John E. Theisinger* and Robert D. Braun†

Georgia Institute of Technology, Atlanta, Georgia 30332-0150

DOI: 10.2514/1.41136

A framework has been developed to identify hypersonic entry aeroshell shapes that are Pareto-optimal with respect to multiple conflicting objectives. The objectives and constraints are derived from the aeroshell geometry and aerodynamic performance. Shapes are parameterized using nonuniform rational B-splines for maximum design flexibility. Hypersonic aerodynamic objectives and constraints are based on rapid predictions obtained from Newtonian flow theory. Single- and multi-objective genetic algorithms are employed for optimization. This framework has been applied to the Mars Science Laboratory mission to quantify tradeoffs inherent to blunt-body aeroshells. Lift-to-drag ratio, volume, and size constraints were derived from the 70-degree sphere-cone aeroshell for this mission, and aeroshell shapes were optimized based on three conflicting objectives: drag area, longitudinal static stability, and volumetric efficiency. First, single-objective optimization revealed the extreme designs for this objective space. Next, two-objective optimization produced Pareto fronts of compromise designs that illustrate the tradeoffs among each pair of objectives. Finally, a three-objective optimization provided Pareto-optimal designs that offer simultaneous improvement in all three objectives relative to the baseline 70-degree sphere-cone aeroshell.

Nomenclature

A	=	reference area, m^2
A	=	axial force, N
$C_D A$	=	drag area (D/q_∞), m^2
$C_L A$	=	lift area (L/q_∞), m^2
$C_M A l$	=	pitching moment per unit freestream dynamic pressure (M/q_∞), m^3
C_p	=	pressure coefficient, $(p - p_\infty)/q_\infty$
D	=	drag force, N
L	=	lift force, N
L/D	=	lift-to-drag ratio
l	=	reference length, m
M	=	pitching moment about the center of gravity, N · m
M	=	Mach number
M_x, M_y, M_z	=	components of aerodynamic moment in aeroshell reference axes system, N · m
m	=	entry system mass, kg
N	=	normal force, N
$\mathbf{n}$	=	surface outward normal unit vector
p	=	static pressure, Pa
q	=	dynamic pressure, Pa
S	=	surface area, m^2
V	=	volume, m^3
$\mathbf{V}$	=	velocity vector, m/s
x, y, z	=	Cartesian coordinates in aeroshell reference axes system, m
Y	=	side force, N
α	=	angle of attack, deg
β	=	ballistic coefficient, kg/m^2
β	=	sideslip angle, deg
$\Delta x_{c.g.}$	=	axial offset in center of gravity, m
$\Delta z_{c.g.}$	=	vertical offset in center of gravity, m
γ	=	ratio of specific heats
η_V	=	volumetric efficiency

Subscripts

max	=	maximum value
trim	=	trimmed value
α	=	derivative with respect to angle of attack, rad^{-1}
0	=	initial value
∞	=	freestream value

I. Introduction

AEROSHELLS are designed to deliver payloads safely through a planetary atmosphere, protecting these payloads from the high aerodynamic heating and loads encountered during hypersonic entry, descent, and landing (EDL). The aeroshell also provides the aerodynamic drag force necessary for deceleration, dissipating approximately 90% of the EDL system's kinetic energy from the point of atmospheric interface. The aeroshell is designed to perform these functions with minimal mass so that useful landed mass is maximized.

An aeroshell generally consists of a forebody (or heat shield), which faces the flow, and a backshell, which completes the encapsulation of the payload. The specific shape of a particular aeroshell is driven by EDL performance requirements and thermal/structural limitations. Four different aeroshell shapes are shown in Fig. 1: the Viking-era 70 deg sphere cone, the Mars Microprobe, the Aeroassist Flight Experiment, and a swept biconic design. Primary drivers of these specific aeroshell designs include drag, stability, nonequilibrium aerothermodynamics, and radiative heating, respectively [1–4]. This diversity in configurations is a direct result of differing mission and flight system requirements: that is, form has followed function in every case.

One fundamental characteristic of an aeroshell is its drag area $C_D A$. Essentially, $C_D A$ represents the amount of drag force that an aeroshell can generate at a given freestream condition (i.e., D/q_∞). During the hypersonic EDL phase, this drag force provides the means of deceleration, suggesting that $C_D A$ should be maximized for a given entry system mass m. The ballistic coefficient is an aeroshell performance parameter that embodies this principle, relating inertial and drag forces, as shown in Eq. (1):

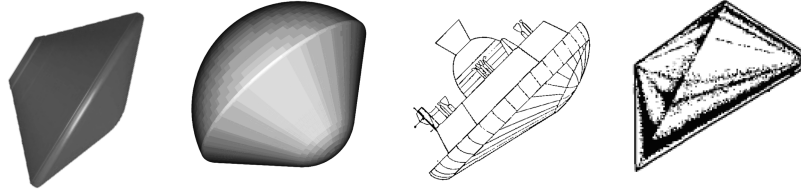$$\beta = \frac{m}{C_D A} \qquad (1)$$

Fig. 1   Various aeroshell shapes [1–4].

A higher β (higher mass per unit drag area) causes EDL events to occur at lower, denser portions of the atmosphere, reducing landed elevation capability and timeline margin. Additionally, peak heat rate and integrated heat load are higher, causing an increase in the thermal loads that the entry system must accommodate. Generally, such accommodations lead to a heavier thermal protection system (TPS) and support structure, reducing the useful landed mass capability of the EDL system.

Another important aeroshell performance parameter is lift-to-drag ratio L/D. A body of revolution, symmetric about its forward axis, will have an L/D equal to zero while flying at an angle of attack α of 0 deg. A body of revolution flying at a nonzero α, or an asymmetric body, however, can produce a nonzero L/D. Motivations for achieving a nonzero L/D aeroshell shape and/or attitude include the following:

1) Reduce the deceleration loads.

2) Increase parachute deployment altitude to enable a higher surface elevation landing site or to increase timeline margin.

3) Provide the capability to control downrange and crossrange, thus facilitating the mitigation of atmospheric uncertainties and improved landing accuracy.

4) Execute an aeroassisted orbit plane change.

5) Relax the approach navigation requirements (i.e., enable a larger entry corridor).

Although a nonzero L/D has distinct advantages, care must be taken not to select an aeroshell shape in which L/D is created at the expense of reducing $C_D A$ and therefore increasing β. This risk is made clear in Eq. (2), in which L/D is written in terms of $C_D A$:

$$L/D = \frac{C_L A}{C_D A} \qquad (2)$$

Consequently, the L/D required of the aeroshell should be set no higher than that necessary to satisfy the mission constraints. An optimal aeroshell shape then achieves this specified L/D while maximizing $C_D A$ (thereby minimizing β). This enables the aeroshell to satisfy an L/D requirement without any unnecessary sacrifice in $C_D A$.

However, if $C_D A$ were maximized in isolation, the resulting aeroshell would be characterized by a flat-plate forebody. Such a shape is impractical from the perspective of other aeroshell objectives and constraints. For example, static stability must exist; this requires a certain amount of sweep in the aeroshell forebody, reducing bluntness and driving the forebody away from a flat plate. This tradeoff between drag and stability is fundamental in aeroshell shape design.

In addition to these aerodynamic considerations, the aeroshell mass should be minimized so that payload mass can be maximized. The aeroshell structure and TPS masses directly affect the amount of payload that the aeroshell can deliver. Other geometric considerations include payload packaging efficiency, volume requirements, and the overall aeroshell size (which is constrained by the launch vehicle shroud).

Aeroshell shape optimization involves multiple conflicting objectives. Therefore, many different optimal solutions exist, each representing a particular compromise, or tradeoff, among these objectives. In the absence of specified preference-weightings for each objective, it is useful to have multi-objective optimization methods that produce diverse sets of optimal solutions. Such

information enables the designer to quantify tradeoffs among conflicting objectives.

II.   Methodology

This work is divided into three main components: hypersonic aerodynamic analysis, shape parameterization, and multi-objective optimization. The following sections detail each component and discuss how these components were integrated to perform multi-objective aeroshell shape optimization.

A.   Hypersonic Aerodynamics

Hypersonic aerodynamic quantities are computed from a surface C_p distribution obtained using the Newtonian theory of fluid flow [5,6]. This theory models the flow as a stream of particles, each particle impacting the surface and completely transferring its normal component of momentum to the surface. Areas of the surface inclined away from the flow are assumed to be "shadowed" from the flow and have a C_p value of zero. Such a model is appropriate for steady, continuum, inviscid, hypersonic flows and becomes more accurate in the combined limit of $M_\infty \to \infty$ and $\gamma \to 1$. As a conceptual design tool, Newtonian theory provides a reasonable approximation of the surface pressure distribution over hypersonic vehicles: a notion that is corroborated by numerous examples in the literature (see [5,6]). Its use is therefore suitable here for estimating the effects of geometry modifications on aeroshell aerodynamic characteristics.

To apply Newtonian theory, an aeroshell surface is discretized into a mesh of surface panels and a C_p distribution is obtained through application of Eq. (3) to each panel:

$$C_p = \begin{cases} C_{p,\max} \left(\frac{\mathbf{V}_\infty}{|\mathbf{V}_\infty|} \cdot \mathbf{n} \right)^2 & \text{for } \mathbf{V}_\infty \cdot \mathbf{n} < 0 \\ 0 & \text{for } \mathbf{V}_\infty \cdot \mathbf{n} \geq 0 \end{cases} \qquad (3)$$

Numerical integration then gives estimates of the aerodynamic force and moment coefficients for the aeroshell. The reference axes for the aeroshell and the corresponding force and moment conventions used for these aerodynamic analyses are shown in Fig. 2.
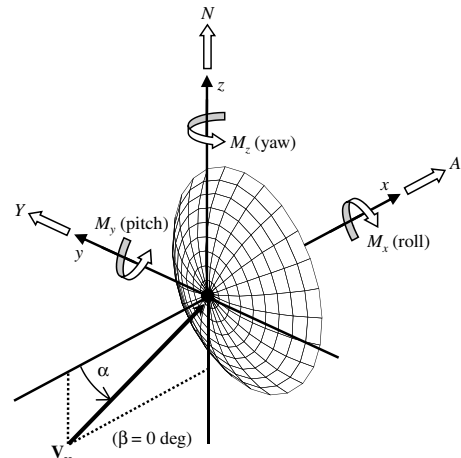

Fig. 2   Aeroshell reference axes system and the corresponding force and moment conventions.

Straight Newtonian theory is applied, which assumes that $C_{p,\max} = 2$ in Eq. (3) [5,6]. This assumption is often modified by setting $C_{p,\max}$ equal to the stagnation value behind a normal shock wave, causing $C_{p,\max}$ to vary with M_∞ and γ. This modification is a more accurate approximation for blunt bodies in hypersonic flow. However, a change in $C_{p,\max}$ simply scales the entire C_p distribution uniformly, relative to the straight Newtonian prediction. The same aeroshell shape thus evolves during optimization using modified Newtonian theory as would be obtained using straight Newtonian theory (albeit with scaled aerodynamic quantities). Furthermore, modified Newtonian aerodynamics are coupled, through M_∞, to the trajectory flown by a given aeroshell shape. However, variations in $C_{p,\max}$ are small for the large M_∞ associated with hypersonic entry trajectories (which is an illustration of the Mach number independence principle [5,6]). Therefore, the use of straight Newtonian theory without a coupled trajectory analysis (i.e., constant $C_{p,\max} = 2$) is appropriate for aeroshell shape optimization driven by hypersonic aerodynamics.

Certain assumptions are applied to the aeroshell to simplify analyses. First, aeroshells are required to be symmetric across the pitch (x–z) plane, and sideslip angle effects are not considered (i.e., $\beta = 0$ deg for all α). As a result, Y, M_x, and M_z are zero for all α. The restriction of bilateral symmetry is a reasonable one because an aeroshell typically only takes on nonzero α and/or a nonaxisymmetric shape to achieve a nonzero L/D. Second, the aeroshell's center of gravity (c.g.) is initially assumed to coincide with its volume centroid (i.e., c.g.$_0 \equiv$ volume centroid). This is equivalent to assuming that the aeroshell has a uniform packaged density or, more generally, that the payload is distributed in such a way that its resultant c.g. lies at the aeroshell volume centroid. Because payload mass is concentrated in regions with largest volume, it is reasonable to assume the c.g.$_0$ and volume centroid coincide as a first approximation.

For a given α_{trim}, the vertical offset in c.g. ($\Delta z_{\text{c.g.}}$) required to trim the aeroshell is computed based on the pitching moment about c.g.$_0$. Figure 3 illustrates the computation of $\Delta z_{\text{c.g.}}$ and the resultant offset c.g. location required for trim (c.g.$_{\text{trim}}$). From the standpoint of payload packaging, $\Delta z_{\text{c.g.}}$ should be minimized to avoid packaging arrangements that are overly restrictive. No axial offset in c.g. is considered (i.e., $\Delta x_{\text{c.g.}} \equiv 0$).

Longitudinal static stability is assessed about c.g.$_{\text{trim}}$ using a centered finite difference of $C_M Al$ with respect to α to calculate the static stability derivative $(C_M Al)_\alpha$. Using the sign convention for M shown in Fig. 3, $C_M Al$ is positive when causing a nose-up rotation. Therefore, a *negative* value of $(C_M Al)_\alpha$ is required for longitudinal static stability.
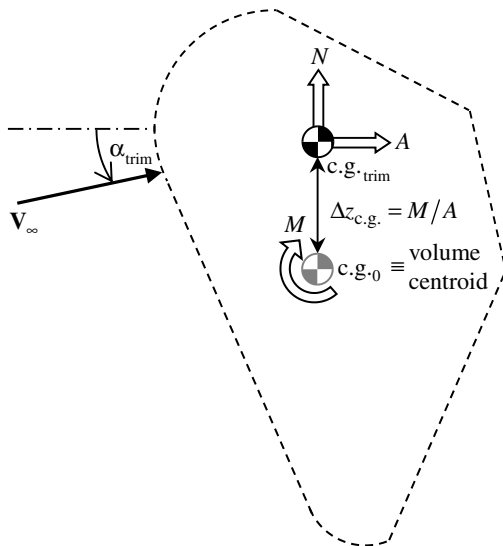
Although lateral (roll) and directional (yaw) static stability can be computed analogously, neither of these quantities is considered herein. A complete study should include an analysis of all three forms of static stability; the current study seeks to explore the tradeoffs between a limited number of design objectives and focuses on the interactions between longitudinal aerodynamic quantities [i.e., $C_D A$, L/D, and $(C_M Al)_\alpha$]. Dynamic stability is also not assessed.

B. Shape Parameterization

The proper choice of shape parameterization is that which yields an appropriate mix of design freedom and computational efficiency. In terms of numerical optimization, it is most computationally efficient to keep the number of design variables to a minimum; however, more design freedom typically requires a larger number of variables. Because aeroshell shapes can vary in complexity based on design requirements, the goal here is to select a shape parameterization that permits sufficient design freedom with a manageable number of variables.

Analytic shapes provide the ability to define an aeroshell in terms of a few geometric parameters, minimizing the number of design variables for optimization while allowing for design and analysis of smooth, manufacturable, and realistic shapes. Examples include the spherically blunted circular cone and the ellipsoidally blunted, raked-off elliptical cone forebodies shown in Fig. 1. The main drawback to this approach is its lack of design freedom: aeroshells are inherently restricted to a specific family of shapes, limiting the variety and generality of possible designs. A more flexible approach is to generate surfaces of revolution (SOR) from spline axial profiles. In this type of parameterization, an axial profile is created from a series of control points and rotated 360 deg about the centerline to form an axisymmetric aeroshell surface. These SOR can be used to represent analytic shapes that are axisymmetric (such as the sphere-cone forebody), but they also allow a wide range of nonanalytic shapes. The control points, along with α, are the design variables used for shape optimization. Despite the significant improvement in design freedom over analytic shapes, all SOR aeroshell shapes are, by definition, axisymmetric.

In this work, aeroshell shapes are represented using nonuniform rational B-spline (NURBS) surfaces [7,8]. Overall, B-spline surfaces provide significant flexibility with a reasonably small number of design variables. Furthermore, NURBS surfaces provide the ability to represent both analytic quadric surfaces and arbitrary free-form surfaces. Surfaces are defined by specifying the locations of control points that form a bidirectional net of control points. Further control is achieved through specification of weights (placed on each control point) and knot values (which define the parameter rectangle over which each control point influences the surface). The NURBS formulation also has two important geometric properties: 1) the convex hull property, which ensures that the surface lies within the convex hull created by the control points, and 2) the local support property, which ensures that each control point only affects a localized region of the surface. Given these two properties, the designer can readily predict the surface shape based on its control net, as the control net forms a planar polyhedral approximation to the surface. Overall,

Fig. 3 Determination of aeroshell c.g.$_{\text{trim}}$ (symmetry plane shown).
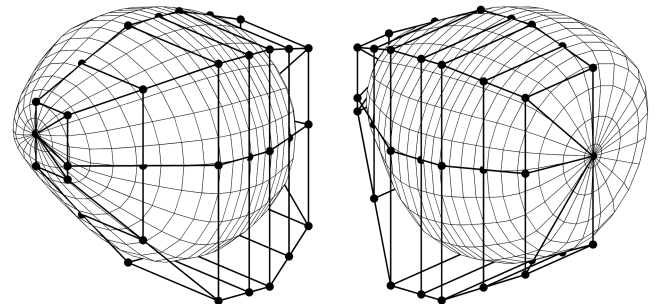

Fig. 4 Oblique front and rear views of an example NURBS surface, shown with control net.

the NURBS surface formulation provides a high degree of shape control and is an intuitive framework for interactive shape design.

An example NURBS aeroshell surface based on the formulation used in this work is shown in Fig. 4. A cubic × quadratic surface provides the desired amount of design flexibility for roughly 20 design variables, including control point locations, their weights, and α. Knot values are held fixed. Constraints are imposed on control point locations such that resulting shapes are convex. Only half of the control net needs to be defined because all aeroshells in this investigation are symmetric across the pitch plane (see Sec. II.A). Control points are distributed axially from the apex of the forebody to the apex of the backshell, totaling five different convex axial control point profiles that define one-half of the aeroshell. The forebody and backshell apex can be moved anywhere vertically along the forebody and backshell, respectively. This NURBS surface is therefore defined by multiple axial profiles rather than a single profile as in the SOR case. Once defined, the control net is mirrored across the pitch plane to form a complete aeroshell surface. The fact that NURBS can exactly represent quadric surfaces provides an advantage in terms of constraint enforcement. Each control point cross section (parallel to the y–z plane shown in Fig. 2) is constrained within a circular envelope, presuming a cylindrical launch vehicle shroud. Once a maximum length and radius are defined, control point placement and weight specifications yield a complete aeroshell surface.

C. Multi-Objective Aeroshell Shape Optimization

In this section, potential objectives and constraints for multi-objective aeroshell shape optimization are presented, followed by a description of the specific optimization framework that has been developed.

1. Aerodynamic Objectives and Constraints

Once an aeroshell surface and α have been specified, aerodynamic characteristics are determined using Newtonian theory, as described in Sec. II.A. These characteristics include $C_D A$, $(C_M Al)_\alpha$, L/D, and $\Delta z_{c.g.}$. Based on reasoning discussed previously (see Secs. I and II.A), the current motivation prescribes an optimization problem in which L/D is used as a constraint, $C_D A$ is maximized, required $\Delta z_{c.g.}$ is minimized (in absolute value), and static stability is maximized by *minimizing* the quantity $(C_M Al)_\alpha$.

2. Geometric Objectives and Constraints

Additional objectives and constraints are computed directly from the aeroshell geometry. Volume V and surface area S are easily computed once the aeroshell geometry is defined and generated using NURBS surfaces. A requirement on V is then checked directly, and additional objectives can be derived from combinations of V and S.

Payload packaging efficiency refers to the distribution of volume (and therefore payload) within the aeroshell surface and can be quantified as a ratio between V and S. A high payload packaging efficiency is defined as the ability to enclose a prescribed payload (indicating a certain V requirement) with minimum structural mass (a limitation on S). This statement contains the assumption that aeroshell structural mass is directly proportional to S, with a proportionality constant equal to an average structural areal density. This simplified model is used in conceptual aeroshell sizing to estimate structural mass from a known S and an areal density based on historical data [9]. The parameter that embodies this definition of packaging efficiency is the volumetric efficiency η_V, defined in Eq. (4) [10]:

$$\eta_V = 6\sqrt{\pi}\,\frac{V}{S^{3/2}} \qquad (4)$$

Note that η_V is maximized at unity for a sphere, which is the aeroshell shape with the best η_V. As such, slender aeroshell shapes generally have a lower η_V and therefore a higher structural mass than blunt aeroshells (for a given V). Additionally, lower η_V indicates a poorer ability to package payload into the aeroshell.

An objective related to TPS mass is not formulated in this investigation, apart from the objective to maximize $C_D A$ and thereby minimize β. Although reducing β reduces both heat rate and heat load (and thus TPS requirements), this is a trajectory effect, in that a lower β leads to a reduced freestream velocity at a given altitude (freestream density). The *local* aerothermodynamic environment at every point on the surface is a function of aeroshell geometry (e.g., surface curvature) as well as freestream conditions. No aerothermodynamic analysis is performed here.

3. Optimization

As mentioned in Sec. I, an optimization problem based on multiple conflicting objectives has many different optimal solutions, each representing a particular compromise, or tradeoff, among these objectives. Each of these optimal solutions is termed *Pareto-optimal*, and in objective space, the set of Pareto-optimal solutions forms the Pareto front. Thus, along the Pareto front, no objective can be improved without degrading another (i.e., a tradeoff occurs). Note that if a pair of objectives does not conflict, then the dimensionality of the objective space can be reduced by eliminating one of those objectives from the multi-objective optimization.

Both single- and multi-objective optimization algorithms can be employed to generate the Pareto-optimal solutions that comprise the Pareto front. In particular, single-objective optimization is useful for locating the extremes of the Pareto front that correspond to each objective. The population-based nature of evolutionary multi-objective algorithms enables many Pareto-optimal solutions to be obtained in a single execution, as opposed to methods that convert the multi-objective optimization problem into a single-objective optimization problem and produce only one Pareto-optimal solution per execution.

The iSIGHT® [11] software package provides a multi-island genetic algorithm (MIGA) [11] for single-objective optimization and the nondominated sorting genetic algorithm (NSGA-II) [12] for multi-objective optimization. Modules were developed in MATLAB® [13] that perform aeroshell shape generation and aerodynamic analyses. These modules are integrated within the iSIGHT optimization framework to provide evaluation of objectives and constraints. The design variables are the locations and weights of NURBS control points and α. The range of possible solutions is limited by constraints such as L/D, V, and overall size.

The MIGA operates like a traditional single-objective genetic algorithm but divides the total population of solutions into subpopulations, or islands. Genetic operations are performed separately on each island. Periodically, individuals are selected from each island and migrated to different islands to maintain diversity and prevent premature convergence. Constraints are handled external to the algorithm through a penalty function.

The NSGA-II is able to treat multiple objectives simultaneously. Initially, a random parent population is created and then sorted into successive nondominated fronts based on their objective values. Each solution is assigned a rank equal to its nondominated front. A crowding distance is computed within each front to differentiate between solutions of the same rank (a diversity-preserving operation). Genetic operations are then performed on the parent population to create an offspring population. The parent and offspring are combined (an elite-preserving operation) and the combined population is sorted and ranked. A new parent population is selected and the steps repeat until termination. The final result is a diverse set of Pareto-optimal solutions. Constraints are handled using binary tournament selection, during which two solutions are chosen from the population and either one of the following occurs:

1) The best solution is selected from the two feasible solutions.
2) The one feasible solution is selected.
3) The solution with the smallest constraint violation is selected from the two infeasible solutions.

III. Results

The Mars Science Laboratory (MSL) aeroshell was chosen as a baseline with which to explore the capabilities developed in this
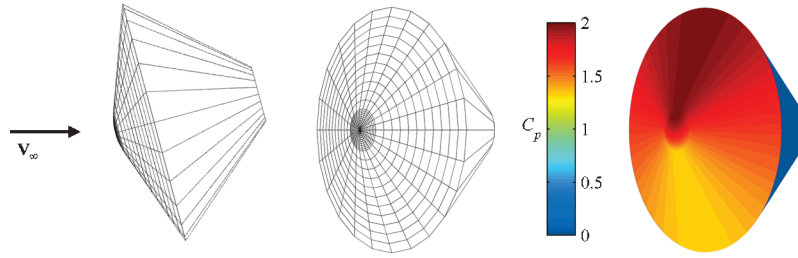
Fig. 5 Baseline aeroshell, illustrating shape and Newtonian C_p distribution at $\alpha_{\text{trim}} = -15.5\,\text{deg}$.

work. Aerodynamic and geometric constraints were derived from published MSL geometry and mission requirements [14]. An analytic MSL-derived aeroshell is shown in Fig. 5. It has a 70 deg sphere-cone forebody with a conical backshell and is intended to fly at a nonzero α, thereby producing an L/D of 0.24. Note that the actual MSL backshell has a biconic geometry; the single conical frustum used here has an equivalent volume. There is a maximum-diameter constraint of 4.5 m dictated by the diameter of the launch vehicle fairing and the size of the integration and test facilities at the Jet Propulsion Laboratory. An aeroshell V requirement of approximately 18 m^3 was determined from the present MSL design. A maximum length constraint was determined based on the total length of the MSL aeroshell, which has a forebody length of approximately 0.75 m and a backshell length of approximately 2 m. Thus, an optimized aeroshell is required to fit within a 4.5-m-diam by 2.75-m-length circular cylinder, have a volume of 18 m^3, and achieve an L/D of 0.24. All of these constraints are to be met by the multi-objective optimization problem.

Initial results revealed that the constraint-handling approach used in the NSGA-II is too severe for imposing equality constraints on V and L/D. In general, these equality constraints greatly reduce the feasible region of the design space. Given this restricted design space, a random initial population will likely consist of entirely infeasible solutions. In accordance with the NSGA-II constraint-handling approach, any feasible solution is selected over any infeasible solution. Once a single feasible design is found (satisfying both equality constraints), a set of Pareto-optimal solutions crowd around this single design as the selection of feasible solutions overpowers the crowding distance penalty. Therefore, the use of equality constraints with the NSGA-II formulation essentially resulted in a single optimal design. To avoid this issue, each equality constraint is replaced by two inequality constraints. In this work, the V and L/D equality constraints were both relaxed by 10% of the original equality-constraint value: V was constrained between 18 and 19.8 m^3 and L/D was constrained between 0.24 and 0.264.

To highlight the tradeoffs associated with this particular application, the following three objectives were selected for aeroshell shape optimization: $C_D A$, $(C_M A l)_\alpha$, and η_V. The analytic baseline aeroshell shown in Fig. 5 was analyzed using the same Newtonian aerodynamics routine that would be employed for optimization. First, the α_{trim} required to produce an L/D of 0.24 was determined. At this value of α_{trim}, the $C_D A$, $(C_M A l)_\alpha$, and η_V were computed. These values serve as a baseline against which to compare solutions produced through optimization and are shown in Table 1.

A. Single-Objective Optimization

Initially, single-objective optimization was performed using the MIGA optimizer to establish the bounding cases for these three objectives. Figure 6 shows the aeroshells produced by the three single-objective optimizations, and Table 2 includes quantitative comparisons with the baseline (Table 1).

The maximum $C_D A$ solution (see Fig. 6a) is an aeroshell with a flat-plate forebody, as expected. The α_{trim} produces the required L/D, and the backshell fulfills the entire V constraint. Because a Newtonian aerodynamic analysis is performed, the backshell is in the shadow region and its shape is arbitrary, given that it satisfies the V constraint. This solution shows that the maximum improvement in $C_D A$ that can be expected is approximately 14%, relative to the baseline. [Note that every percentage increase in $C_D A$ translates into a decrease in β by the same percentage for a fixed m, as shown by Eq. (1). Alternatively, every percentage increase in $C_D A$ translates into an increase in m by the same percentage for a fixed β.] Both the $(C_M A l)_\alpha$ and η_V have worsened relative to the baseline, with a larger adverse impact being on $(C_M A l)_\alpha$. Effectively, drag has been improved to the point that this aeroshell is statically unstable.

The aeroshell that maximizes longitudinal static stability will minimize $(C_M A l)_\alpha$ (recall that this quantity takes on a negative value for statically stable configurations). Figure 6b shows the solution obtained from the single-objective optimization to minimize $(C_M A l)_\alpha$, resulting in an improvement of approximately 60% relative to the baseline. Contrary to the maximum $C_D A$ solution, the volume has been shifted into the forebody and distributed such that the forebody has a more slender, swept character. As expected, the two ignored objectives have worsened relative to the analytic baseline, with $C_D A$ decreasing by approximately 27% relative to the baseline.

Finally, the solution for maximizing η_V alone is shown in Fig. 6c. Because V is set as a constraint, maximizing η_V is equivalent to minimizing S [see Eq. (4)]. The resulting ellipsoidal shape of the aeroshell achieves a very high η_V, with an improvement of approximately 34% relative to the baseline. Furthermore, the optimizer achieves this maximum η_V at the lower boundary of the

Table 1 Objective and constraint values for baseline aeroshell

Parameter	Value
$C_D A$, m^2	25.56
$(C_M A l)_\alpha$, m^3/rad	−12.18
η_V	0.7343
L/D	0.240
V, m^3	18.0

Table 2 Comparison between the aeroshells produced by single-objective optimization and the baseline

Parameter	Maximum $C_D A$		Minimum $(C_M A l)_\alpha$		Maximum η_V	
	Value	% difference	Value	% difference	Value	% difference
$C_D A$, m^2	29.20	+14%	18.57	−27%	8.715	−66%
$(C_M A l)_\alpha$, m^3/rad	0.4006	+103%	−19.51	−60%	−2.008	+84%
η_V	0.6990	−5%	0.6596	−10%	0.9816	+34%
L/D	0.240	0%	0.240	0%	0.240	0%
V, m^3	19.6	+9%	18.0	0%	18.1	+1%

a) Maximum $C_D A$
(α_{trim} = -13.7 deg)

b) Minimum $(C_M A l)_\alpha$
(α_{trim} = -25.5 deg)

c) Maximum η_V
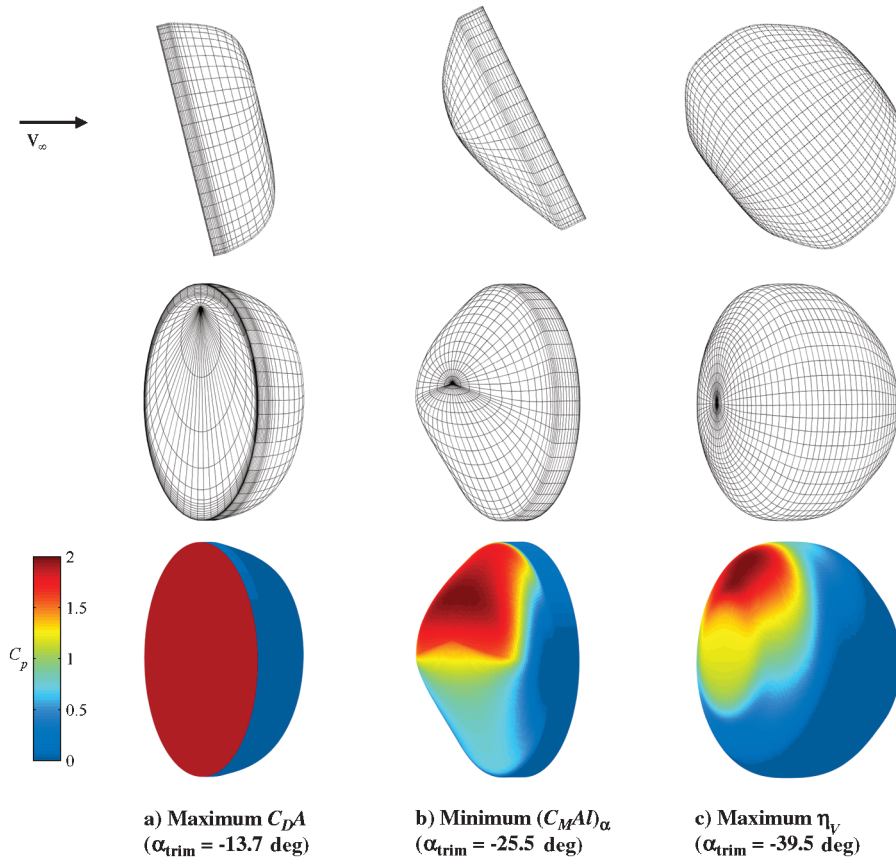(α_{trim} = -39.5 deg)

Fig. 6   Aeroshells produced by single-objective optimization, illustrating shape and Newtonian C_p distribution at α_{trim}.

volume constraint (18 m³). Note that although a spherical aeroshell would have the theoretical maximum η_V, the L/D and size constraints force deviations from an actual 18 m³ sphere. Once again, the other two objectives have been significantly worsened by optimizing only a single objective, with $C_D A$ decreasing by approximately 66% relative to the baseline. This sacrifice in $C_D A$ is more than twice that for the minimum $(C_M A l)_\alpha$ case.

B.   Multi-Objective Optimization

1.   Two-Objective Optimization

As shown through single-objective optimization, the three chosen objectives conflict in terms of what exactly constitutes an optimal aeroshell shape. Without explicit preferences for each objective, many possible tradeoff solutions exist. The solutions obtained in the previous section are themselves Pareto-optimal. They represent the extremes of the Pareto fronts and correspond with maximum possible tradeoffs. Using the NSGA-II, a set of Pareto-optimal solutions was generated for each pair of objectives by performing two-objective optimization. These solutions are shown as Pareto fronts in Figs. 7–9, displayed along with the results from the single-objective optimizations and the baseline for comparison. The utopia solution is also shown for each pair of objectives, indicating the (unattainable) ideal improvement in both objectives.

All three Pareto fronts are continuous and convex, having the following characteristics in common:

1) The single-objective solutions bound the Pareto front. The coverage of the Pareto front shows the potential range of variation in the pair of objectives as tradeoffs occur.
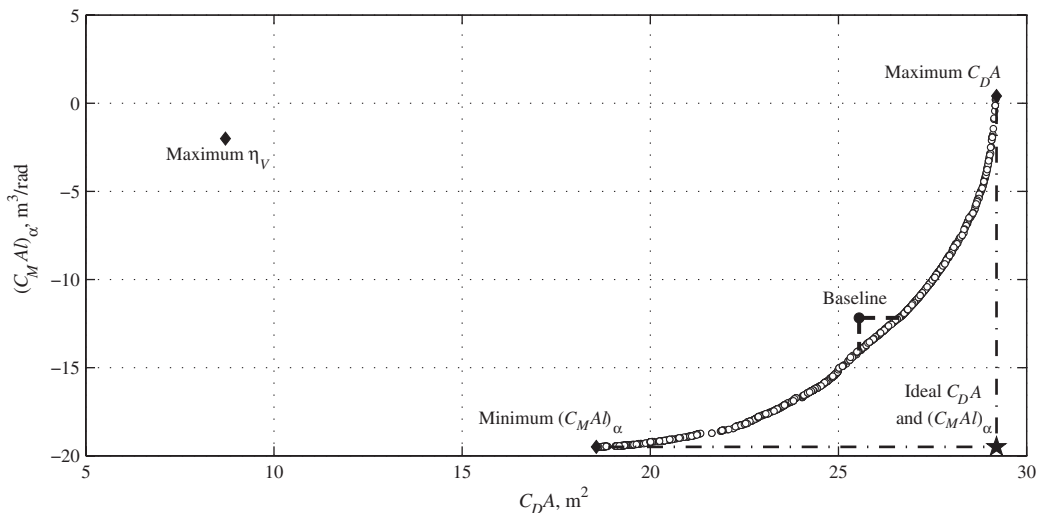

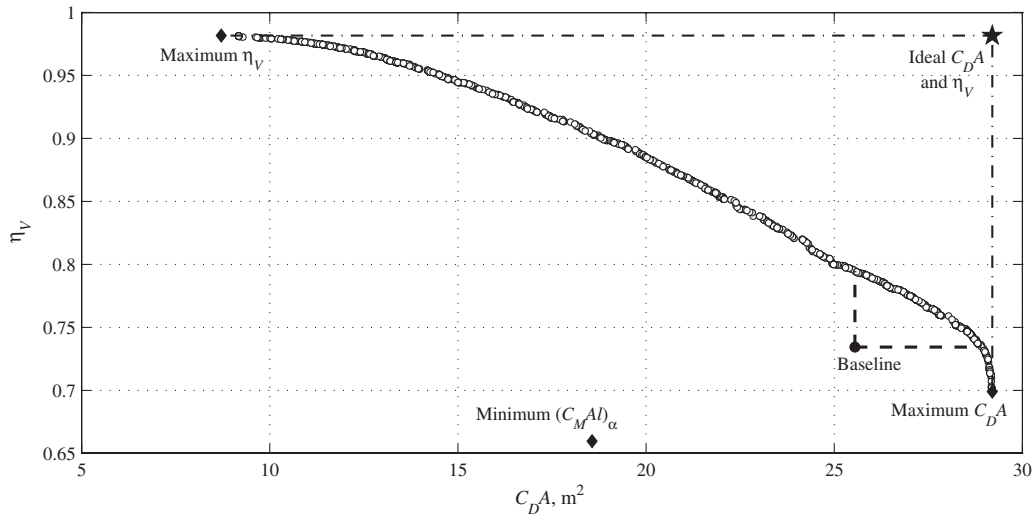Fig. 7   Pareto-optimal solutions for maximizing $C_D A$ and minimizing $(C_M A l)_\alpha$.

Fig. 8 Pareto-optimal solutions for maximizing $C_D A$ and maximizing η_V.

2) The slope along the Pareto front indicates the strength of tradeoff between the pair of objectives. Starting from the single-objective solution for one objective and moving along the Pareto front, the tradeoff in that objective is weakest at first and increases until becoming strongest at the single-objective solution for the other objective. This behavior results from the convex shape of these Pareto fronts.

3) The baseline does not lie along the Pareto front: it is a solution that is dominated by all the other Pareto-optimal solutions. Furthermore, a 90 deg arc drawn from the baseline solution toward the Pareto front identifies Pareto-optimal solutions that provide an improvement in *both* objectives, relative to the baseline.

Figure 7 shows the Pareto-optimal set of solutions that demonstrates the tradeoff between $C_D A$ and $(C_M A l)_\alpha$. In terms of aeroshell shape, the tradeoff in $(C_M A l)_\alpha$ for additional $C_D A$ is due to the flattening or blunting of the forebody with an attendant shift of volume into the backshell. This shift in volume has a destabilizing effect.

Figure 8 shows the Pareto-optimal set of solutions that demonstrates the tradeoff between $C_D A$ and η_V. Compared with the Pareto front in Fig. 7, this Pareto front extends over a much wider range of $C_D A$ values, as the results show that it is possible to sacrifice much more $C_D A$ when maximizing η_V than when minimizing $(C_M A l)_\alpha$. In terms of shape, aeroshells with high η_V tend to lack broad, flat forebody surfaces that are characteristic of

aeroshells with high $C_D A$; this is not necessarily the case for aeroshells with high $(C_M A l)_\alpha$, as evidenced by the aeroshell in Fig. 6b.

Finally, Fig. 9 shows the Pareto-optimal set of solutions that demonstrate the tradeoff between η_V and $(C_M A l)_\alpha$. In terms of shape, the tradeoff in $(C_M A l)_\alpha$ for η_V results from the overall redistribution of the volume in the aeroshell as η_V is increased. This shifting of volume into the backshell has a destabilizing effect (similar to what occurs as $C_D A$ is increased). A comparison with Figs. 7 and 8 shows the following:

1) A somewhat greater sacrifice in $(C_M A l)_\alpha$ is possible for maximization of $C_D A$ than for maximization of η_V.

2) A somewhat greater sacrifice in η_V is possible for minimization of $(C_M A l)_\alpha$ than for maximization of $C_D A$.

The first statement asserts that a flat-plate forebody is most destabilizing as it forces all of the volume to be shifted from the forebody into the backshell. The maximum η_V aeroshell has a relatively even distribution of volume between the forebody and backshell, maintaining a small amount of static stability. The second statement asserts that maximizing static stability produces the worst η_V, because $(C_M A l)_\alpha$ dictates the shape of both the forebody and backshell, neither of which provides much η_V in the case of minimized $(C_M A l)_\alpha$. The maximum $C_D A$ flat-plate forebody aeroshell, on the other hand, allows for the possibility of a backshell with higher η_V.
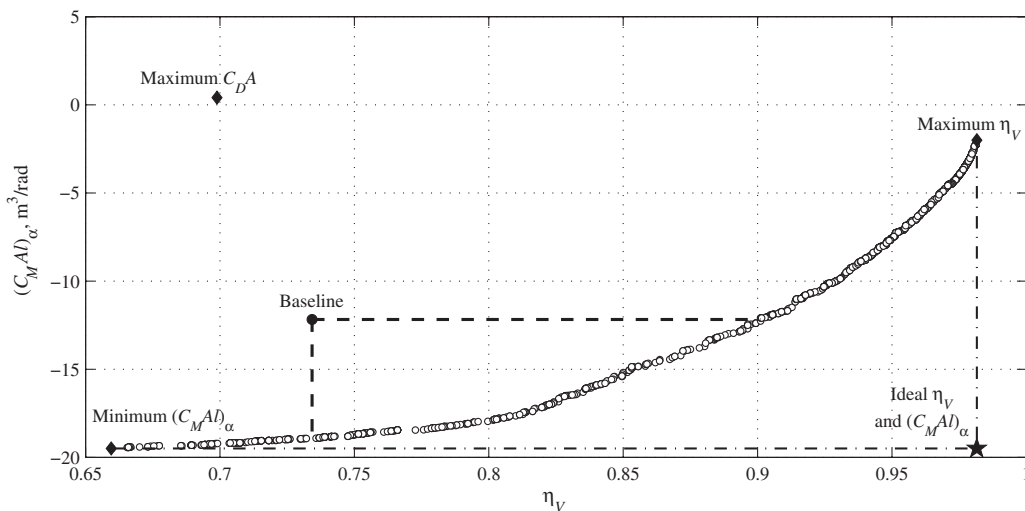

Fig. 9 Pareto-optimal solutions for maximizing η_V and minimizing $(C_M A l)_\alpha$.

$\mathbf{V}_\infty$

C_p

a) Improvement in both
$C_D A$ **and** $(C_M Al)_\alpha$
$(\alpha_{trim}$ **= -16.2 deg)**

b) Improvement in both
$C_D A$ **and** η_V
$(\alpha_{trim}$ **= -14.2 deg)**

c) Improvement in both
η_V **and** $(C_M Al)_\alpha$
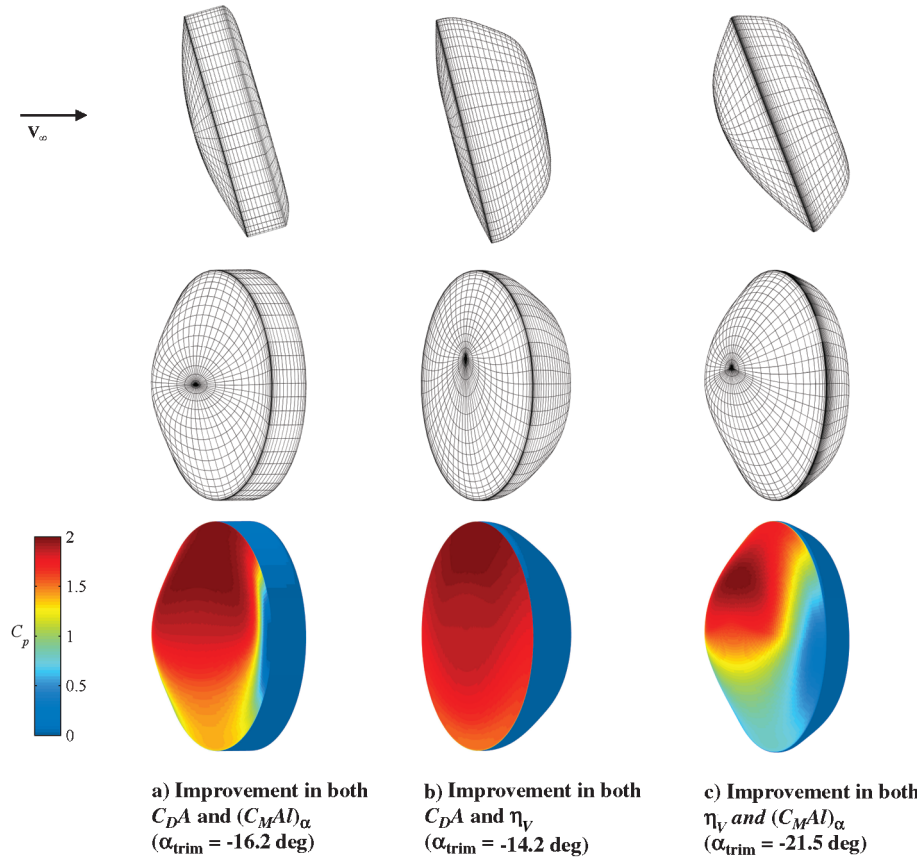$(\alpha_{trim}$ **= -21.5 deg)**

Fig. 10   Aeroshells produced by two-objective optimization, illustrating shape and Newtonian C_p distribution at α_{trim}.

As previously indicated, there is a segment along each Pareto front containing numerous solutions that provide improvement in both objectives, relative to the baseline. To investigate this aspect of the objective space further, a single design was selected from each of these segments. The three resulting designs are shown in Fig. 10. In Table 3, the objective and constraint values for each aeroshell are compared with those of the baseline (Table 1).

The design in Fig. 10a shows an improvement in both $C_D A$ and $(C_M Al)_\alpha$, with a greater improvement in $(C_M Al)_\alpha$. Compared with the baseline aeroshell, the forebody has been blunted slightly and the backshell is shallower, improving the $C_D A$ and $(C_M Al)_\alpha$, respectively. Note that the η_V has been degraded relative to the baseline.

Next, Fig. 10b shows an aeroshell that provides an improvement in both $C_D A$ and η_V. Compared with the baseline, this aeroshell has a blunter forebody that increases $C_D A$ and a backshell with a more rounded character that serves to increase the overall η_V. Note that a portion of this increased η_V is possibly due to increased V; this aeroshell has reached the upper boundary of that constraint with a value of 19.8 m³. The static stability of this aeroshell has been degraded significantly, relative to the baseline.

Finally, Fig. 10c shows an aeroshell that provides simultaneous improvement in both η_V and $(C_M Al)_\alpha$. Compared with the base-

line, the $C_D A$ has been degraded significantly, as volume has been shifted into the forebody, thus providing improvements in η_V and $(C_M Al)_\alpha$ at the expense of surface area that is blunt to the freestream. The backshell is shallow and swept (a hybrid of the two backshells shown in Figs. 10a and 10b), because η_V and $(C_M Al)_\alpha$ are the primary drivers of backshell shape. Note, once again, that V has approached the upper boundary of its constraint, potentially providing some of the improvement in η_V over the analytic baseline. Overall, however, the internal volume is being used more efficiently in terms of Eq. (4).

2.   Three-Objective Optimization

From the preceding discussion, it is clear that designs exist that offer improvement over the baseline in terms of each pair of objectives. The natural progression is to determine whether designs exist that offer improvement in *all three* objectives. Thus, three-objective optimization was performed using the NSGA-II. Three inequality constraints were added to this problem (one for each objective) requiring that all objectives perform at least as well as the values shown in Table 1 for the baseline aeroshell.

Figure 11 displays the results of this optimization, and an example design from this set of solutions is shown in Fig. 12. This aeroshell is compared with the baseline in Table 4. Each solution in Fig. 11

Table 3   Comparison between the aeroshells produced by two-objective optimization and the baseline

Parameter	Improvement in both $C_D A$ and $(C_M Al)_\alpha$		Improvement in both $C_D A$ and η_V		Improvement in both η_V and $(C_M Al)_\alpha$	
	Value	% difference	Value	% difference	Value	% difference
$C_D A$, m²	25.81	+1%	28.04	+10%	18.04	−29%
$(C_M Al)_\alpha$, m³/rad	−13.59	−12%	−7.99	+34%	−15.43	−27%
η_V	0.6780	−8%	0.7590	+3%	0.8466	+15%
L/D	0.241	0%	0.241	0%	0.252	+5%
V, m³	18.7	+4%	19.8	+10%	19.6	+9%

Fig. 11 **Pareto-optimal solutions for maximizing C_DA, maximizing η_V, and minimizing $(C_MAl)_\alpha$.**

Table 4 **Comparison between the aeroshell produced by three-objective optimization and the baseline**

Parameter	Value	% difference
C_DA, m^2	26.50	+4%
$(C_MAl)_\alpha$, m^3/rad	−12.45	−2%
η_V	0.7477	+2%
L/D	0.241	+0%
V, m^3	18.1	+1%

represents an improvement over the baseline in terms of all three objectives and is Pareto-optimal with respect to every other solution in this figure. Based on Fig. 11, the tradeoffs among the three objectives are consistent with the tradeoffs identified through two-objective optimization. The strongest tradeoff here is between C_DA and $(C_MAl)_\alpha$: at a fixed η_V, the decrease in C_DA as $(C_MAl)_\alpha$ improves is more extreme than the decrease in C_DA as η_V improves at a fixed $(C_MAl)_\alpha$. Further investigation into these results showed that many of the improvements in η_V corresponded with an increase in V; essentially, the optimizer exploited the flexibility built into the constraint on V.

The example solution shown in Fig. 12 has a V and L/D close to that of the analytic baseline and shows a small improvement in all three objectives. The aeroshell forebody is similar to that of a spherical segment, but has a slightly elliptical contour near the nose. This blunted forebody provides improved C_DA. The backshell is more rounded and shallower than that of the baseline aeroshell, providing improved η_V and $(C_MAl)_\alpha$.

The single-objective cases presented in Fig. 6 indicate that the maximum possible improvement in C_DA, $(C_MAl)_\alpha$, and η_V is approximately 14, 60, and 34%, respectively. However, constraining each objective such that none can be degraded below those of the baseline prevents these maximum improvements from being attained. Figure 11 shows that an approximately 4% increase in C_DA is expected to be the maximum achievable improvement over the baseline, without degrading the other two objectives. Similarly, Fig. 11 shows that the maximum improvement in $(C_MAl)_\alpha$ is expected to be approximately 12% and the maximum improvement in η_V is expected to be approximately 6%. Many Pareto-optimal solutions exist that provide improvements intermediate to these three extremes; the selection of a particular compromise solution will depend on the preferences of the designer and the specific mission requirements.

IV. Conclusions

A method to perform multi-objective aeroshell shape optimization has been developed. The nonuniform B-spline surface formulation is used to represent the aeroshell shapes because it allows a wide diversity of complete aeroshell shapes while maintaining a relatively low number of control points (or design variables) for optimization. Newtonian flow theory is used to rapidly assess hypersonic aerodynamic performance of candidate aeroshells.

An optimization framework has been constructed that enables use of single- and multi-objective evolutionary algorithms to generate Pareto-optimal sets of solutions. Objectives and constraints are determined based on the aerodynamic performance and geometry of the aeroshell. They include drag area, longitudinal static stability, lift-to-drag ratio, c.g. offset, volumetric efficiency, volume, and overall aeroshell size.

After deriving design constraints based on the MSL mission, single- and multi-objective optimization was performed using drag area, longitudinal static stability, and volumetric efficiency as objectives and lift-to-drag ratio, volume, and size constraints. Results revealed solutions that offer improvement in these objectives relative to the analytic 70 deg sphere cone, which has been employed by all U.S. robotic Mars missions. These sets of Pareto-optimal solutions also served to highlight the fundamental tradeoffs between drag area, longitudinal static stability, and volumetric efficiency.

References

[1] Braun, R. D., and Manning, R. M., "Mars Exploration Mars Exploration Entry, Descent and Landing Challenges," 2006 IEEE Aerospace Conference, Inst. of Electrical and Electronics Engineers Paper 1076, Mar. 2006.

[2] Mitcheltree, R. A., DiFulvio, M., Horvath, T. J., and Braun, R. D., "Aerothermal Heating Predictions for Mars Microprobe," AIAA Paper 98-0170, Jan. 1998.

[3] Syvertson, C. A., "Research Problems in Atmosphere Entry and Landing for Manned Planetary Missions," NASA TN D-4977, Jan. 1969.

[4] Jones, J. J., "The Rationale for an Aeroassist Flight Experiment," AIAA Paper 87-1508, June 1987.

[5] Anderson, J. D., *Hypersonic and High Temperature Gas Dynamics*, 2nd ed., AIAA Education Series, AIAA, Reston, VA, 2006, pp. 54–63, 70–71, 73–74, 292, 299–300, 326–327, 341–346.
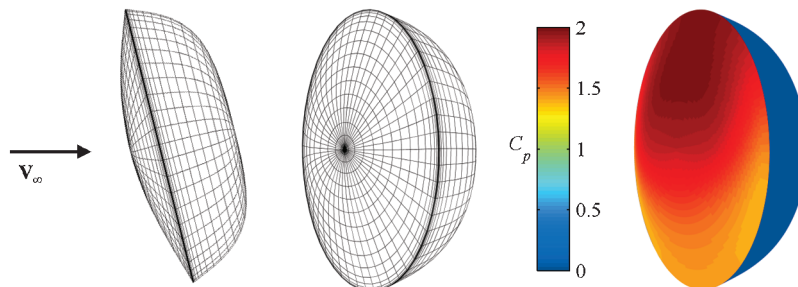

Fig. 12 **Aeroshell produced by three-objective optimization, illustrating shape and Newtonian C_p distribution at $\alpha_{\text{trim}} = -14.9$ deg.**

[6] Bertin, J. J., *Hypersonic Aerothermodynamics*, AIAA Education Series, AIAA, Reston, VA, 1994, pp. 277–287.

[7] Piegl, L., and Tiller, W., *The NURBS Book*, 2nd ed., Springer–Verlag, Berlin, 1997, pp. 128–136.

[8] Rogers, D. F., *An Introduction to NURBS: With Historical Perspective*, Academic Press, New York, 2001, pp. 179–184, 209–226.

[9] Dyke, E. R., "Planetary Probe Mass Estimation Tool Development and Its Application to Titan Aerocapture," AIAA Paper 2003-4956, July 2003.

[10] Hankey, W. L., and Elliott, G. A., "Hypersonic Lifting Body Optimization," *Journal of Spacecraft and Rockets*, Vol. 5, No. 12, Dec. 1968, pp. 1463–1467.
doi:10.2514/3.29503

[11] iSIGHT, Software Package, Ver. 10.0, Engineous Software, Inc., Cary, NC, 2006.

[12] Deb, K., Agrawal, S., Pratap, A., and Meyarivan, T., "A Fast and Elitist Multi-Objective Genetic Algorithm: NSGA-II," *IEEE Transactions on Evolutionary Computation*, Vol. 6, No. 2, 2002, pp. 182–197.
doi:10.1109/4235.996017

[13] MATLAB, Software Package, Ver. R2008b, The MathWorks, Inc., Natick, MA, 2008.

[14] Edquist, K. T., Dyakonov, A. A., Wright, M. J., and Tang, C. Y., "Aerothermodynamic Environments Definition for the Mars Science Laboratory Entry Capsule," AIAA Paper 2007-1206, Jan. 2007.

O. de Weck
Associate Editor